https://doi.org/10.5194/egusphere-2026-3056
Preprint. Discussion started: 9 July 2026

LACRIT: an automated lidar framework for detecting cirrus and contrails and retrieving their radiative properties

Andres E. Bedoya-Velásquez [1], Claire Sarrat [2], Céline Parzani [2], and Romain Ceolato [1]

[1]ONERA, DOTA, Université de Toulouse, 31000, Toulouse, France
[2]ONERA, DTIS, Université de Toulouse, 31000, Toulouse, France

Correspondence: Andres E. Bedoya-Velásquez (andres.bedoya@onera.fr)

Abstract. The accurate retrieval of radiative properties for cirrus and contrail-induced clouds remains a significant challenge, particularly in the optically thin and subvisible regimes where molecular scattering dominates and signal-to-noise constraints are critical. We present a layer-based retrieval framework for Cloud Optical Depth (COD) and Lidar Ratio (LR) utilizing complementary ground-based observations from a co-located elastic–depolarization lidar, microwave radiometer, and all-sky camera deployed in Toulouse, France. Here, COD is retrieved using a transmittance method grounded in robust log-median statistics applied to molecular reference windows. Subsequently, a modified version of the particular-integration formulation is employed to retrieve LR, ensuring consistent altitude indexing between normalized signal ratios and the physical molecular profile. The close agreement observed between transmittance-based and particular-integration CODs, with relative differences lower than 4%, underscores the internal consistency and numerical stability of the retrieval method across a broad range of optical depths, including subvisible cloud systems with COD lower than 0.05.

When applied to representative cirrus and contrail cases, the framework reveals significant variability in retrieved LR for similar COD, highlighting the sensitivity of LR to factors such as cloud altitude which is linked with thermodynamic conditions and microphysical state of the cloud ice crystals. Nearly-fresh contrails display lower LR and depolarization around 23% which is consistent with expected ice-particle evolution. This proposed framework offers a solid foundation for long-term monitoring of cirrus and contrail radiative properties, as well as for evaluating model parameterizations of aviation-induced cloudiness.

1 Introduction

Contrails represent a major source of non-CO_2 anthropogenic climate forcing associated with aviation (Li and Groß, 2025). When persistent, aircraft condensation trails can evolve into contrail-induced cirrus, modifying cloud coverage, optical depth, and the atmospheric radiative transfer. These processes introduce substantial uncertainty into estimates of aviation's climate impact, as the formation, persistence, and radiative properties of contrails depend sensitively on ambient thermodynamic conditions and ice-cloud microphysics. Despite their recognized importance, contrail–cirrus interactions remain one of the least constrained components of aviation climate forcing, limiting the development of robust mitigation strategies.

Aerosol-related climate effects are commonly categorized into aerosol–radiation interactions (ARI), which alter radiative fluxes through scattering and absorption, and aerosol–cloud interactions (ACI), which modify cloud microphysical and macro-

https://doi.org/10.5194/egusphere-2026-3056
Preprint. Discussion started: 9 July 2026

physical properties. Persistent contrails constitute a specific and complex subset of ACI, as they originate from aircraft exhaust water vapor and aerosols and may transition from freshly formed ice particles into optically thin or dense cirrus clouds. During this evolution, ice particles undergo growth, aggregation, and habit changes, leading to strong variability in extinction, backscatter, and depolarization properties. This temporal evolution significantly complicates their representation in climate models and contributes to large uncertainties in radiative forcing estimates (Bock and Burkhardt, 2019; Lee et al., 2021).

The optical and microphysical properties of cirrus and contrails have been investigated for several decades using both in-situ and remote-sensing approaches. A comprehensive synthesis by Schumann and Heymsfield (2017) compiled more than 200 observational studies, documenting contrail lifetimes, ice number concentrations, geometrical thickness, optical depth, and extinction. However, in-situ observations remain inherently limited by spatial coverage, flight safety constraints, and sampling representativeness, particularly for aged or spatially extended contrail cirrus. These limitations motivate the use of ground-based and space-borne remote sensing techniques, which provide continuous, range-resolved observations over extended time periods.

Among remote sensing methods, lidar observations have proven especially valuable for characterizing contrails and cirrus clouds either from satellites and ground-based platforms (Li and Groß, 2025; Comstock and Sassen, 2001). Elastic and Raman lidars enable the retrieval of key cloud radiative properties, including cloud optical depth, extinction, lidar ratio, and volume linear depolarization ratio, the latter being particularly sensitive to ice-crystal shape and orientation. Early studies by Freudenthaler et al. 1996 demonstrated the potential of polarization lidar measurements to discriminate ice-cloud microphysics and to track the temporal evolution of contrails. Subsequent investigations have further exploited depolarization measurements to distinguish between spherical and nonspherical ice particles, assess habit variability, and identify specular reflection effects associated with horizontally oriented crystals (Noel et al., 2002; Chepfer et al., 2004; Hlavka et al., 2012; Dionisi et al., 2013; Kustova et al., 2022).

To retrieve cirrus and contrail radiative and microphysical properties from lidar observations different methodologies has been developed (Gil-Díaz et al., 2024; Cadet et al., 2005; Mitchell et al., 2025; Martucci et al., 2010). These include transmittance-based approaches, Klett and Fernald inversions, Raman techniques, and combined elastic–depolarization retrievals. Each method offers complementary strengths and limitations, depending on factors such as cloud optical thickness and signal-to-noise conditions (Ansmann et al., 1992; Platt et al., 1994; Immler and Schrems, 2007; Dionisi et al., 2013). Robust layer detection, accurate determination of cloud boundaries, and reliable estimation of extinction and lidar ratio remain central challenges, particularly for optically thin or subvisible cirrus where molecular scattering dominates the signal.

The increasing availability of high-quality observational datasets has also supported the development and validation of contrail and cirrus models, such as the Contrail Cirrus Prediction (CoCiP) model (Schumann, 2012) and automated contrail detection algorithms based on satellite imagery (Ng et al., 2024). Studies by Kärcher et al. 2009 and Schumann and Heymsfield 2017 demonstrate that improved observational constraints are essential for refining model parameterizations of contrail formation, persistence, and radiative impact. In this context, advanced lidar-based retrieval frameworks provide a critical link between observations and models, enabling detailed evaluation of contrail microphysical evolution and its radiative consequences.

https://doi.org/10.5194/egusphere-2026-3056
Preprint. Discussion started: 9 July 2026

The objective of this study is to contribute to this effort by developing and applying a robust, layer-based lidar retrieval framework that combines elastic backscatter, depolarization measurements, and synergistic observations to characterize the radiative properties of both natural cirrus and contrail-induced clouds. By focusing on optically thin and subvisible cloud regimes, where uncertainties remain large, this work aims to (i) improve the detection and geometrical characterization of contrail and cirrus layers, (ii) retrieve consistent estimates of cloud optical depth and lidar ratio under low signal-to-noise conditions, and (iii) assess the sensitivity of these properties to contrail age and thermodynamic environment. The resulting analysis provides new observational constraints relevant for the evaluation of contrail–cirrus representations in climate models and for reducing uncertainties in aviation-induced radiative forcing.

The manuscript is organized as follows. Section 2 describes the observational site and the co-located instrumentation used in this study, including the lidar system, microwave radiometer, and all-sky camera. Section 3 introduces the layer-based detection algorithm (LACRIT), and the methodology for retrieving cloud radiative properties from lidar observations. Section 4 presents the main results, including the analysis of representative cirrus and contrail cases and the evaluation of retrieved optical and microphysical properties. Finally, Section 5 summarizes the main findings and outlines perspectives for future work.

2 Site and instrumentation

ONERA, the French Aerospace Lab, is a research institute with various operational sites across France. The facilities located in Toulouse, Occitanie, in southern France (N: 43.3412, E: 1.2824) are dedicated to this project. The Optics and Associated Techniques Department (DOTA), one of the key departments, specializes in research in the field of optronics, benefiting sectors such as aeronautics, space, defense security, environmental studies, astronomy, and medical imaging. To enhance the understanding of light-matter interactions in the atmosphere, a suite of remote sensing instruments has been established on the rooftop of the DOTA-Toulouse building, which has been operational for the past six years. The co-located instrumentation, illustrated in Fig. 1, includes a microwave radiometer, a dual-channel CIMEL lidar, and an all-sky all-sky camera.

2.1 CIMEL-376GPN Lidar

The lidar system used in this study is a micro-pulse lidar manufactured by CIMEL Electronique (model CE376). This instrument belongs to the new generation of compact, eye-safe elastic lidars designed for continuous and autonomous monitoring of aerosols and clouds in the troposphere and lower stratosphere. The CE376 routinely provides observations up to altitudes of approximately 15–20 km, with a vertical resolution of 15 m and a temporal resolution of 1 min, making it well suited for the detection of optically thin cirrus and contrail layers.

The system operates at two wavelengths: 532 nm, equipped with polarization-sensitive detection enabling the retrieval of volume linear depolarization ratio, and 808 nm for complementary elastic backscatter measurements. The laser source operates in eye-safe mode, emitting pulse energies of approximately 7 μJ at 532 nm and 4 μJ at 808 nm, with a repetition rate of 4.6 kHz. These characteristics ensure a high signal-to-noise ratio while allowing unattended, continuous operation.

https://doi.org/10.5194/egusphere-2026-3056
Preprint. Discussion started: 9 July 2026

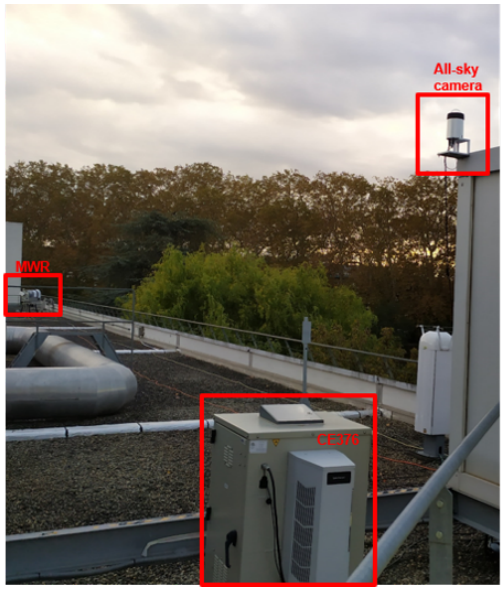

Figure 1. Co-located instrumentation at ONERA Toulouse site.

Backscattered radiation is collected in a biaxial configuration using two Galilean telescopes, optimizing near-range performance and overlap characteristics. Signal detection is performed with avalanche photodiodes (APDs) operating in photon-counting mode, providing high sensitivity to weak atmospheric returns. Data acquisition and instrument control are fully automated via dedicated software, enabling long-term deployments and consistent data quality. For a detailed description of the instrument, refer to Popovici et al., 2018, and Sanchez Barrero et al., 2024

2.2 OMEA 3C all-sky camera

The OMEA 3C offers a comprehensive hemispheric view of the sky, featuring a field of view measuring 180° x 180°. To enhance image processing, a geometric calibration is conducted to establish the pixel-to-azimuth/zenith conversion matrix. This calibration was executed by tracking the trajectories of 10 different stars, pinpointing their coordinates over time, and then following the detailed procedure outlined in Antuña-Sánchez et al., 2022, using the ORION tool as illustrated in Fig. 2. Based on the azimuth/zenith matrix, the cartesian coordinates of each pixel are calculated on a 2D cartesian plan (x,y,z) with:

$$\begin{cases} x = \rho \sin\varphi \cos\theta \\ y = \rho \sin\varphi \sin\theta \\ z = \rho \cos\varphi \end{cases} \tag{1}$$

Where ρ represent the altitude of the cirrus / contrail. The variables θ and ϕ denote the azimuth and zenith angles, respectively. Only pixels with a zenith angle of 80° or less are retained, as those with higher zenith angles are too far from the camera

https://doi.org/10.5194/egusphere-2026-3056
Preprint. Discussion started: 9 July 2026

to be considered. The outcome is a projection of the image, as illustrated in Fig. 2. After the projection is completed, highlights are filtered to enhance the contrast and visibility of the contrails in the images. This projection is attached to the contrails altitude that in this work is determined by lidar.

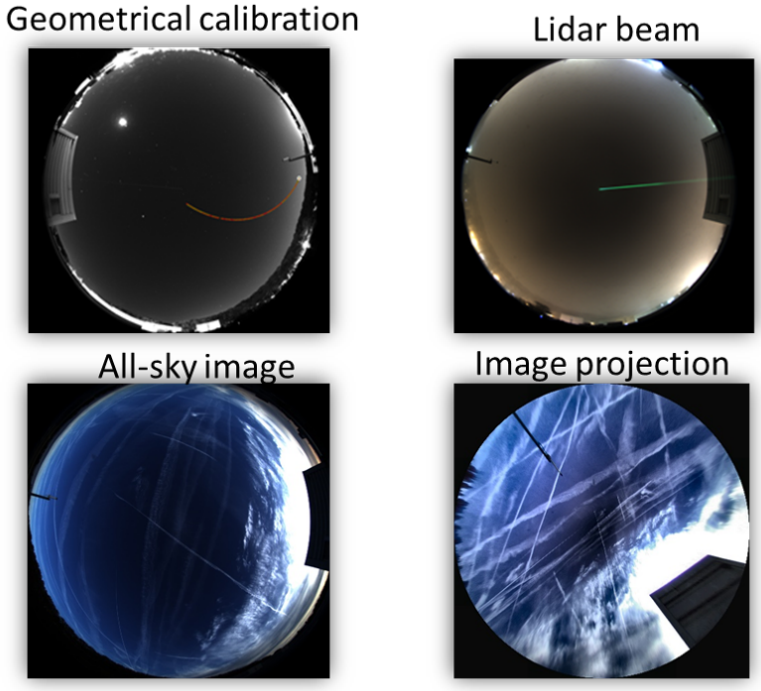

Figure 2. All-sky camera preprocessing. Top: geometric calibration of the fisheye image. Bottom: raw hemispherical image (left) and corresponding Cartesian projection (right)

The calibration and 2D projection of the images were serve also to determine the Lidar beam coordinates, namely latitude: 43.6°and longitude: 1.5°. This information is used to track the contrail's position relative to the Lidar field of view.

2.3 RPG-HATPRO Microwave radiometer

The gound-based microwave radiometer (RPG-HATPRO-G2, Radiometer Physics GmbH) is used as a passive remote-sensing instrument to continuously measure atmospheric brightness temperatures associated with oxygen and water vapor. Oxygen emissions are observed in the extended K-band between 51 and 58 GHz, while water vapor and cloud liquid water are measured in the V-band from 22 to 31 GHz. The radiometer exhibits a typical radiometric resolution of 0.3–0.4 K (RMS error) for an integration time of 1 s. Observations are performed continuously and fully automatically using a multi-elevation scanning strategy. Brightness temperatures are measured at six elevation angles (90.0°, 42.0°, 30.0°, 19.2°, 10.2°, and 5.4°), corresponding to air masses of approximately 1.0, 1.5, 2.0, 3.0, 5.6, and 10.6, respectively. This multi-angle configuration enhances the vertical sensitivity of the measurements and enables the retrieval of thermodynamic atmospheric profiles, including temper-

https://doi.org/10.5194/egusphere-2026-3056
Preprint. Discussion started: 9 July 2026

ature and humidity profiles, as well as integrated water vapor (IWV) and liquid water path (LWP). These products are used here as complementary constraints to the lidar observations for the characterization of cloud and contrail thermodynamic environments.

3 Layer-based automatic algorithm to cirrus – contrail detection using lidar

To enable the automatic detection of cirrus and contrail layers and the retrieval of their radiative properties, we developed a layer-based inversion framework called LACRIT (Lidar-based Automatic CiRrus and contrail Identification Tool). The framework is designed to operate with elastic lidar observations, and its processing workflow is illustrated in Fig. 3.

To facilitate the interpretation of this workflow, the algorithm is described sequentially following the main processing steps: (i) Data preprocessing (Fig. 3, PREPROCESSING), (ii) Cloud-layer detection and transmittance-based optical depth (Fig. 3, CLOUD DETECTION and TRANSMITTANCE METHODS), and (iii) Lidar ratio retrieval (Fig. 3, Lidar Ratio RETRIEVAL).

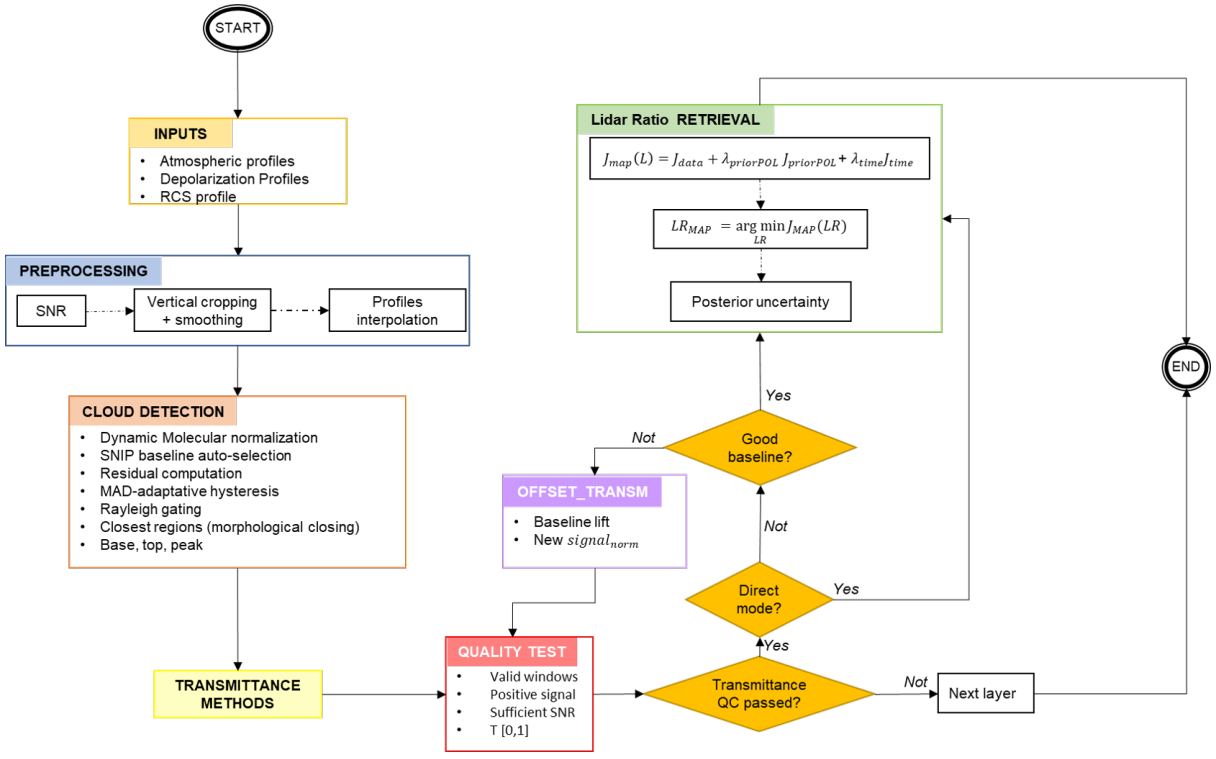

Figure 3. Block-diagram of the Layer-based inversion framework algorithm, LACRIT.

https://doi.org/10.5194/egusphere-2026-3056
Preprint. Discussion started: 9 July 2026

The primary input to the algorithm is the elastic range-corrected signal (RCS), which is treated throughout the processing chain as a normalized proxy of the attenuated backscatter profile. This treatment is justified because most algorithmic operations rely on normalized ratios, differential quantities, or estimates of atmospheric transmittance, for which the unknown system calibration constant effectively cancels out. As a result, the retrieval can be performed without requiring absolute radiometric calibration. Absolute quantities are only recovered during the inversion stage when the normalized elastic signal is combined with molecular reference profiles using consistent altitude indexing.

Cloud layers are first identified from the normalized elastic backscatter profiles using a residual hysteresis detection method. The procedure relies on a molecular baseline estimated with a Non-linear Iterative Peak-clipping (SNIP) algorithm, which provides a robust representation of the background molecular signal. Significant positive residuals relative to this baseline are then detected through adaptive thresholding and morphological filtering, allowing the identification of vertically coherent cloud structures. Once cloud layers are identified, their radiative properties are retrieved through a combination of transmittance-based optical depth estimation and lidar-ratio inversion.

Following layer detection, the retrieval stage estimates a set of *cloud radiative properties (CRP)* together with geometrical characteristics of the detected layers. These quantities include the *cloud optical depth (COD)*, the *lidar ratio (LR)*, vertically resolved extinction profiles, the geometrical thickness of the layer, and the cloud base, peak, and top altitudes.

When available, thermodynamic profiles from a *microwave radiometer (MWR)* are used to compute the molecular reference and to provide contextual information about the thermodynamic environment of the detected cloud layers. If MWR data are not available, the molecular reference profile is calculated using pressure and temperature profiles derived from a scaled standard atmosphere or reanalysis data (e.g., ERA5). All thermodynamic profiles are interpolated onto the lidar altitude grid and used to refine the computation of the molecular backscatter profile.

At each time step, the input variables consist of (i) the normalized RCS profile, (ii) a molecular backscatter profile $\beta_{\mathrm{Ray}}(r)$, (iii) the altitude grid r, and (iv) the volume linear depolarization ratio (VLDR), when available, which is primarily used for cloud-type characterization. The analysis is restricted to a molecular-dominated altitude interval $[r_{\min}, r_{\max}]$ in order to reduce the influence of boundary-layer aerosols and to avoid regions with very low signal-to-noise ratio (SNR) at high altitudes.

3.1 Data preprocessing

The retrieval is based on elastic lidar measurements expressed by the standard single-scattering lidar equation:

$$P(R) = \frac{K\,O(R)}{R^2}\,\beta(R)\,\exp\left[-2\int_0^R \alpha(r)\,dr\right], \tag{2}$$

where $P(R)$ is the received power at range R, K is the system constant (laser energy, receiver efficiency, detector gain), $O(R)$ is the overlap function, and $\beta(R)$ and $\alpha(R)$ denote the volume backscatter and extinction coefficients, respectively (molecular and aerosol contributions). As mentioned, the measured profiles are handled as RCS signals, $S(R) = P(R)\,R^2$, which reduces the geometric $1/R^2$ spreading and facilitates the identification of atmospheric layers.

https://doi.org/10.5194/egusphere-2026-3056
Preprint. Discussion started: 9 July 2026

The input to the algorithm consists of the elastic RCS profiles at the working wavelength, a co-registered molecular reference profile $\beta_{\mathrm{Ray}}(R)$ computed from thermodynamic information (MWR/sonde/model), and the volume linear depolarization ratio VLDR profiles, all interpolated onto a common altitude grid. Profiles are temporally averaged (typically 1–5 min), vertically smoothed, and restricted to a molecular-dominated altitude interval above the boundary layer in order to minimize aerosol contamination and overlap-related effects.

The VLDR profiles are post-processed to derive a representative cloud-core value while minimizing biases associated with noise, molecular background contamination, and vertical sampling effects. Rather than relying on single-bin extrema or simple averaging near the layer peak, a physically defined core region is constructed for each detected cloud layer. This core is centered on the retrieved peak altitude and spans a fixed vertical window (peak $\pm$ Δr), ensuring that the analysis focuses on the portion of the layer most representative of the dominant ice particle population.

For cloud detection and transmittance estimation only, both the elastic RCS and the Rayleigh reference are normalized over a high-altitude molecular interval $[r_1, r_2]$, selected such that particulate backscatter is negligible and the signal is dominated by Rayleigh scattering, so using Eq. 2, the measured range-corrected signal:

$$S(R) \propto O(R)\,\beta(R)\,\exp\left[-2\int_0^r \alpha(r)\,dr\right]$$

is normalized over a molecular reference interval $[r_1, r_2]$:

$$\tilde{S}(R) = \frac{S(R)}{\langle S(r)\rangle_{r\in[r_1,r_2]}}. \tag{3}$$

This normalization largely cancels multiplicative factors in Eq. 2 (e.g., K and slowly varying gain terms) and reduces sensitivity to absolute calibration, thereby stabilizing residual-based layer detection and the windowed transmittance estimate.

A clear-air molecular baseline $B(R)$ is then estimated from the normalized elastic profile $\tilde{S}(R)$ using a SNIP algorithm, which provides a robust estimate of the background molecular signal in the presence of positive cloud returns. Thus, when sufficient cloud-free bins are available, an additional low-order polynomial fit to the clear-air points is computed and can be used as an alternative baseline for the modified particular integration method calculations.

3.2 Cloud-layer detection and transmittance-based optical depth

Cloud layers are identified from a residual field defined relative to the molecular baseline:

$$Res(r) = \frac{y_{\mathrm{norm}}(r) - B(r)}{|B(r)| + \varepsilon}, \tag{4}$$

where $y_{\mathrm{norm}}(r)$ denotes the normalized elastic backscatter profile and $B(r)$ represents the molecular baseline estimated using the SNIP algorithm. The parameter ε is a small regularization constant introduced to avoid numerical instabilities associated with very small baseline values in clear-air regions. Its value is chosen sufficiently small compared to typical baseline magnitudes so that it does not influence the residual in cloud-containing regions.

https://doi.org/10.5194/egusphere-2026-3056
Preprint. Discussion started: 9 July 2026

The noise level of the profile is estimated from the residual field using the median absolute deviation (MAD), which provides a robust and outlier-resistant estimate of background variability. This noise estimate is then used to define adaptive detection thresholds for cloud identification.

Cloud layers are recognized through a hysteresis-based detection scheme that utilizes two adaptive thresholds: a higher threshold to identify the core of a layer and a lower threshold to expand the detection into adjacent bins. This dual-threshold approach improves sensitivity to optically thin layers while limiting false detections caused by noise. To further reduce spurious detections near molecular signal levels, an optional Rayleigh-consistency criterion is applied, requiring the normalized elastic signal to exceed the normalized molecular reference by a predefined margin.

The resulting binary detection mask is first regularized using a light morphological closing operation, which removes small gaps within detected structures and improves the vertical continuity of potential cloud layers. The regularized mask is then analyzed using connected-component labeling in order to isolate vertically contiguous features. Each connected structure therefore represents a candidate cloud layer. To ensure physical relevance, only those structures exceeding a minimum vertical extent and containing at least one core bin identified by the high detection threshold are retained. For each validated layer, the geometrical properties are subsequently derived by determining the cloud base z_b, the cloud top z_t, and the altitude of the peak backscatter within the layer.

For each identified layer, an initial estimate of the cloud optical depth is obtained using a transmittance method. Two altitude windows are defined: one below the cloud base and one above the cloud top, separated from the cloud boundaries by a safety gap to avoid contamination from cloud-edge effects. The two-way transmittance is estimated using robust log-median statistics:

$$\hat{T} = \exp\Big(\mathrm{median}_{r\in\mathcal{W}_t}\left[\ln\tilde{S}(r)\right] - \mathrm{median}_{r\in\mathcal{W}_b}\left[\ln\tilde{S}(r)\right]\Big), \tag{5}$$

where $\mathcal{W}_b$ and $\mathcal{W}_t$ denote the altitude windows below the cloud base and above the cloud top, respectively, and $\tilde{S}(r)$ is the normalized lidar signal. The corresponding cloud optical depth is then computed as

$$\mathrm{COD}_{\mathrm{trans}} = -\frac{1}{2}\ln\hat{T}. \tag{6}$$

Quality control is applied to ensure the reliability of the transmittance estimate. The checks include verification of signal positivity within the windows, sufficient signal-to-noise ratio, and physical consistency of the resulting transmittance value (i.e., $0 < T \leq 1$).

When residual molecular contamination or baseline bias affects the validity of the transmittance estimate, an adaptive baseline lift is applied (denoted as `OFFSET_TRANSM` in Fig. 3). In this procedure, an additive offset is estimated from a clear-air segment located above the cloud layer and applied to the normalized elastic profile used in the transmittance calculation. The transmittance is then recomputed using the lifted signal. Additional constraints are imposed to ensure that the applied correction remains physically plausible.

https://doi.org/10.5194/egusphere-2026-3056
Preprint. Discussion started: 9 July 2026

3.3 Lidar Ratio Retrieval

The LR is retrieved by scanning a bounded interval of candidate values. For each LR value, extinction profiles are obtained using forward and backward Klett inversions (Klett, 1981, 1985). These inversions yield LR-dependent estimates of the cloud optical depth:

$$\mathrm{COD}_{\mathrm{Klett}}(\mathrm{LR}) = \mathrm{LR} \int_{r_b}^{r_t} \beta_{\mathrm{cloud}}(r)\, dr. \tag{7}$$

In parallel with the Klett inversions, a modified implementation of the particular integration method (PI) proposed by Cadet et al. (2005) is used to estimate the cloud optical depth directly from the normalized elastic signal. For a given candidate LR, the PI optical depth is computed as

$$\mathrm{COD}_{\mathrm{PI}}(\mathrm{LR}) = \mathrm{LR} \int_{r_b}^{r_t} \left(\frac{S_{\mathrm{PI}}(r)}{B_{\mathrm{PI}}(r)} - 1 \right) \beta_{\mathrm{Ray}}(r)\, dr. \tag{8}$$

Here $S_{\mathrm{PI}}(r)$ denotes the normalized elastic backscatter signal used in the PI calculation, while $B_{\mathrm{PI}}(r)$ represents the corresponding molecular baseline estimated from the clear-air reference profile. The ratio term $(S_{\mathrm{PI}}/B_{\mathrm{PI}} - 1)$ therefore expresses the relative excess of the elastic signal above the molecular background and is dimensionless. The quantity $\beta_{\mathrm{Ray}}(r)$ is the physical molecular backscatter coefficient evaluated on the same altitude grid, ensuring dimensional consistency of the integral. When multiple baseline estimates are available (e.g., SNIP or polynomial baselines), the solution producing the smallest mismatch with the transmittance-derived optical depth is retained.

The optimal lidar ratio is determined by enforcing consistency between the optical depth retrieved from the elastic signal and the independent transmittance-based estimate $\mathrm{COD}_{\mathrm{trans}}$. This consistency is expressed through the minimization of a regularized cost function:

$$J(\mathrm{LR}) = \frac{[\mathrm{COD}(\mathrm{LR}) - \mathrm{COD}_{\mathrm{trans}}]^2}{\sigma_\tau^2} + \lambda_{\mathrm{prior}} \frac{[\ln(\mathrm{LR}) - \ln(\mathrm{LR}_0)]^2}{\sigma_{\mathrm{LR}}^2} + \lambda_{\mathrm{time}} \frac{[\ln(\mathrm{LR}) - \ln(\mathrm{LR}_{\mathrm{prev}})]^2}{\sigma_{\mathrm{time}}^2}. \tag{9}$$

The first term measures the mismatch between the cloud optical depth predicted by the LR-dependent retrieval and the transmittance-based estimate. The second and third terms introduce prior and temporal regularization, respectively. In the current implementation, LR_0 and σ_{LR} can be prescribed from a climatological prior, derived from a depolarization-based cloud classification, or estimated from the mean VLDR of the detected layer. This term is weighted by λ_{prior}, allowing the strength of the prior constraint to be adjusted. The temporal regularization term penalizes large deviations from the lidar ratio retrieved at the previous time step, $\mathrm{LR}_{\mathrm{prev}}$, thereby promoting temporal continuity of the solution. Together, these two terms act as soft constraints that stabilize the inversion while still allowing the retrieved LR to adapt to the observed optical depth. The optimal lidar ratio corresponds to the minimum of the cost function within the prescribed LR interval. When both SNIP and

https://doi.org/10.5194/egusphere-2026-3056
Preprint. Discussion started: 9 July 2026

polynomial baselines are available for the PI calculation, the baseline producing the smallest relative mismatch with $\mathrm{COD}_{\mathrm{trans}}$ is retained.

The regularized formulation of the inversion naturally provides access to an a posteriori representation of the solution uncertainty. By interpreting the cost function in a Bayesian framework, the likelihood of candidate lidar-ratio values can be approximated from the shape of the cost function around its minimum. This allows the derivation of a proxy for the posterior distribution of LR and associated optical-depth estimates. Although this uncertainty analysis is implemented within the framework, its detailed evaluation and validation are beyond the scope of the present work and will be addressed in a dedicated future study.

4 Results and discussion

4.0.1 Radiative properties of a multilayer cirrus on 25 December 2022

Retrieving the radiative properties of optically thin contrails and cirrus clouds from lidar observations presents several methodological challenges. One of the most critical issues is accurately determining the geometric boundaries of the clouds. Uncertainties in establishing the cloud's base and top can lead to errors in transmittance, which is essential for most lidar-based retrieval algorithms for clouds (Gil-Díaz et al., 2024; Cadet et al., 2005; Mitchell et al., 2025; Martucci et al., 2010).

As described in Sec. 3, the robustness of the LACRIT algorithm in both cloud-layer detection and radiative property retrieval relies on a carefully constrained set of input parameters that control signal preprocessing, molecular baseline estimation, and adaptive thresholding. In the example case presented here, the analysis is restricted to altitudes above 5 km, ensuring predominantly molecular scattering conditions and minimizing contamination from aerosols. Temporal averaging over 5 min, combined with vertical smoothing over ten range bins, substantially enhances the signal-to-noise ratio while preserving the vertical structure of thin cloud layers. These preprocessing choices, together with the adaptive detection strategy, contribute to a stable and physically consistent identification of cloud boundaries, which is essential for reliable transmittance-based and modified PI retrievals of cloud optical properties.

Table 1 summarizes the key features of the retrieval example shown in Fig. 4. The layer-resolved retrievals provide insight into the variability of the LR between different cloud layers. As illustrated in Fig. 4, the LR varies only slightly between the two detected layers—36 sr at approximately 10.5 km and 38 sr at about 12.6 km—despite differences in COD and VLDR. Such variability is physically plausible for thin cirrus and contrail-like ice clouds, considering their microphysical properties, temperature conditions, and scattering geometry, as reported in the LR distributions of Iwabuchi et al. (2012).

Our results are also consistent with cirrus climatology studies conducted by Dionisi et al. (2013), based on multichannel Raman–Mie–Rayleigh lidar observations, which show that LR is not solely determined by COD. For instance, horizontally oriented ice crystals can produce strong angular scattering anisotropy. Consequently, depending on the viewing geometry and the stability of crystal orientation, extinction may increase without a corresponding increase in backscatter. This can lead to elevated apparent lidar ratios even when the optical depth remains relatively stable or low, as demonstrated by Zhou et al. (2012).

https://doi.org/10.5194/egusphere-2026-3056
Preprint. Discussion started: 9 July 2026

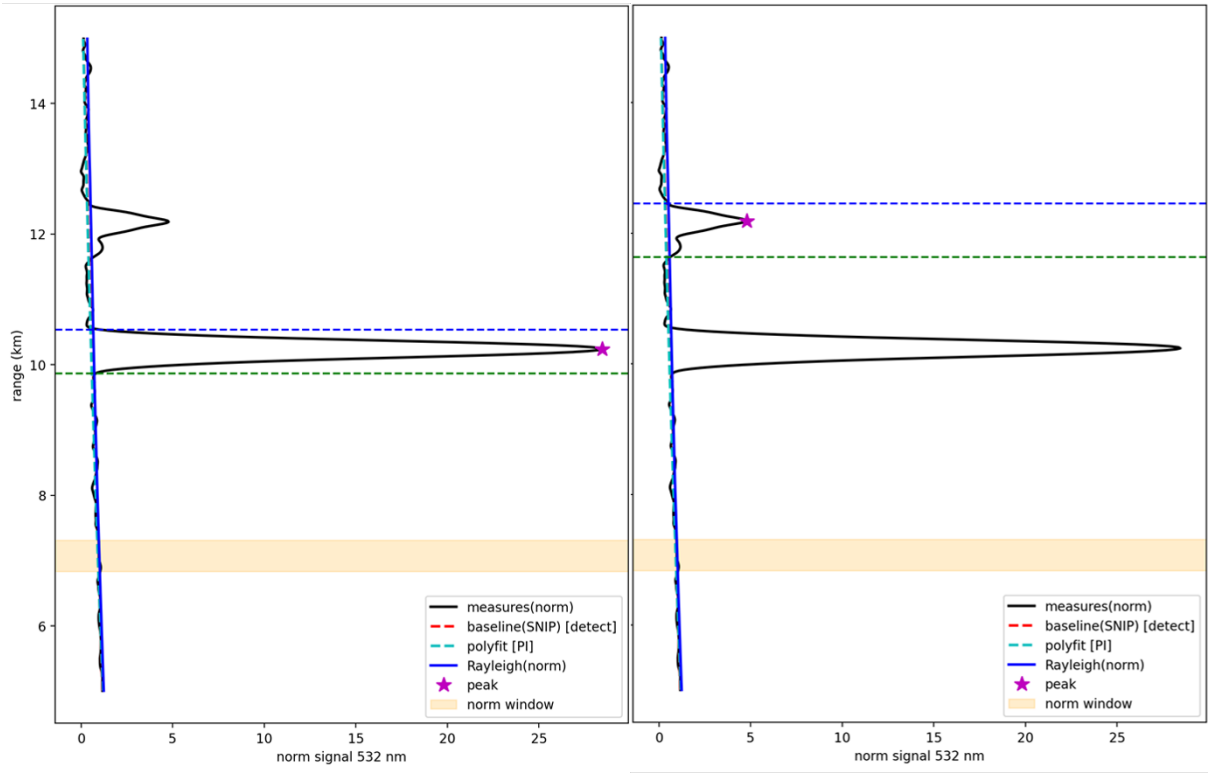

Figure 4. Layer-resolved CRP diagnostics at 11:30 UTC on 25 December 2022. Normalized elastic backscatter profiles at 532 nm (black) are shown together with the SNIP baseline (red dashed), polynomial fit (cyan dashed), and normalized Rayleigh reference (blue). Retrieved cloud base and top are indicated by green and blue dashed lines, respectively, and the magenta star marks the residual peak. The spanned yellow band highlights the automatic Rayleigh zone determined.

Figure 5 provides an overview of the post-processed outputs of the LACRIT algorithm between 07:00 and 13:15 UTC on 25 December 2022. The upper panel shows the time–height evolution of the RCS at 532 nm, highlighting two cirrus layers in the upper troposphere. Vertical shaded bands mark selected profiles that illustrate the different cloud structures. The right panel displays representative vertical profiles extracted at those times, while the lower panels present the temporal evolution of the retrieved CRP for each detected layer, including COD, LR, and VLDR.

The lidar ratio is displayed as a fraction of 100 to preserve the figure scale. The data were averaged over 5-minute intervals, and the error bars represent the standard error of the mean (SEM). The SEM is computed as the standard deviation divided by the square root of the number of samples within each averaging window, representing the uncertainty of the estimated mean rather than the intrinsic variability of the measurements. The periods of low data retrieval in both layer 1 and layer 2 are primarily related to restrictions placed to prevent unphysical outcomes due to low SNR or the detection of extremely thin layers.

https://doi.org/10.5194/egusphere-2026-3056
Preprint. Discussion started: 9 July 2026

Table 1. Summary of cloud optical depth (COD) consistency and lidar ratio (LR) retrieval for the two cirrus layers. The relative mismatch quantifies the agreement between transmittance-based and PI/transmittance COD estimates. The Rayleigh margin Δ_{Ray} denotes the minimum fractional excess of the normalized elastic signal over the molecular (Rayleigh) reference required for a layer core to be detected, thereby limiting noise-driven detections in near-molecular regions. H_{min} is the minimum vertical thickness imposed for a detected layer to be retained, reducing spurious thin features and stabilizing transmittance estimates. Ambient temperature was taken from ERA5.

Layer	COD mismatch [%]	$\mathrm{LR_{PI}}$ [sr]	Altitude [km]	Temperature [°C]	Detection constraints
Layer 1	19.4	36	9.8–10.5	-50 to -55	SNIP-residual detection (normalized signal); Rayleigh-gated core only; $\Delta_{\mathrm{Ray}} = 0.03$; $H_{\mathrm{min}} = 200$ m;
Layer 2	33	38	11.6–12.5	-60 to -65	SNIP-residual detection (normalized signal); Rayleigh-gated core only; $\Delta_{\mathrm{Ray}} = 0.03$; $H_{\mathrm{min}} = 200$ m;

The retrieved CRP reveal a systematic, though moderately dispersed, relationship between COD and VLDR at 532 nm. To characterize this dependence, several nonlinear candidate models were evaluated using the Akaike Information Criterion corrected for finite sample size (AICc), which provides a suitable balance between goodness of fit and model complexity for moderately sized datasets. Among the tested formulations, the *power-law* model provided the best compromise between parsimony and explanatory capability, with parameters $a = 0.56$ and $b = 0.16$, the latter controlling the curvature of the COD–VLDR relationship (Fig. 6). Although the relationship remains scattered, as reflected by the moderate coefficient of determination ($R^2 = 0.37$), the model captures the first-order tendency of the dataset while remaining more parsimonious than more flexible nonlinear alternatives.

The moderate level of explained variance indicates that while COD exerts a first-order control on VLDR, a substantial fraction of the variability arises from microphysical properties not directly represented by optical depth. These include variations in ice-crystal habit, particle size distribution, preferred orientation, and viewing geometry. Consequently, VLDR tends to be particularly sensitive to microphysical variability in subvisible to thin cirrus clouds, whereas its sensitivity to further increases in optical depth diminishes as clouds become optically thicker.

The resulting relationship therefore reflects a sublinear increase of VLDR with COD: depolarization increases with optical depth but at a progressively weaker rate. This behavior is consistent with the observed trend, where the strongest VLDR variations occur in optically thin clouds, while at larger COD values the relationship gradually flattens toward a weak-slope regime rather than a strict saturation plateau. Similar gradual saturation behavior has been widely reported for cirrus and contrail-induced clouds and is often attributed to the predominance of randomly oriented ice crystals together with enhanced multiple-scattering effects (Yorks et al., 2011; Zhou et al., 2012; Urbanek et al., 2018).

https://doi.org/10.5194/egusphere-2026-3056
Preprint. Discussion started: 9 July 2026

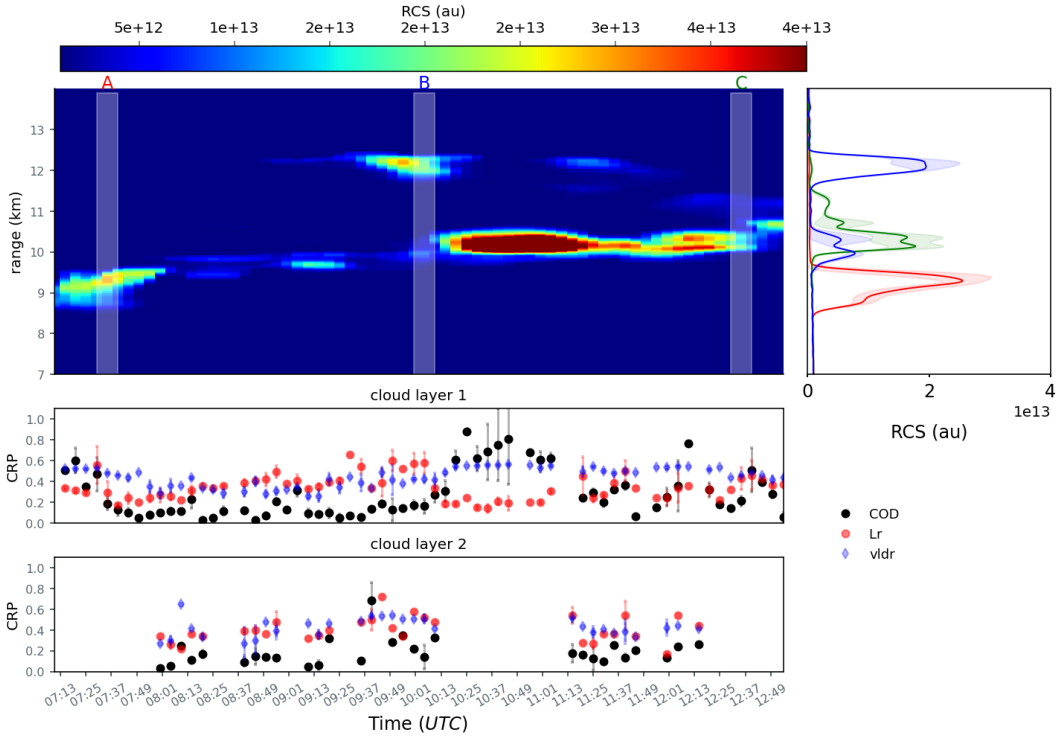

Figure 5. The time-height evolution of the range-corrected signal (RCS) at 532 nm on 25 December 2022 is presented alongside the retrieved cloud radiative properties from the LACRIT algorithm. The upper panel highlights two persistent upper-tropospheric cirrus and contrail layers in the RCS. Vertical shaded bands (A–C) indicate selected time intervals for detailed profile diagnostics, with the corresponding mean vertical profiles displayed on the right. The lower panels illustrate the temporal evolution of cloud optical depth (COD), the lidar ratio (LR), displayed as LR/100 for scaling purposes, and the mean volume linear depolarization ratio (VLDR) for each detected layer. The time series of CRP were averaged over 5-minute intervals, and the error bars represent the standard error of the mean.

In optically thin ice clouds, small increases in ice number concentration, particle shape complexity, or preferred orientation can significantly influence the polarized backscatter signal. By contrast, as optical depth increases, additional increases in COD produce progressively smaller changes in depolarization due to enhanced extinction. In this regime, multiple scattering, particle aggregation, and the increasing prevalence of randomly oriented crystals progressively limit the sensitivity of VLDR to further increases in COD. These processes are not explicitly considered in the present work, given the nature of the cases analyzed; however, they constitute an important avenue for future studies aimed at evaluating the sensitivity of the method under optically thicker cloud conditions.

4.0.2 Contrail case detected on 06 September 2025

Leveraging the co-located instrumentation described in Sect. 2, we present a representative case study of an isolated contrail that intersected the lidar field of view between 06:30 and 06:45 UTC on 06 September 2025. This period is particularly well

https://doi.org/10.5194/egusphere-2026-3056
Preprint. Discussion started: 9 July 2026

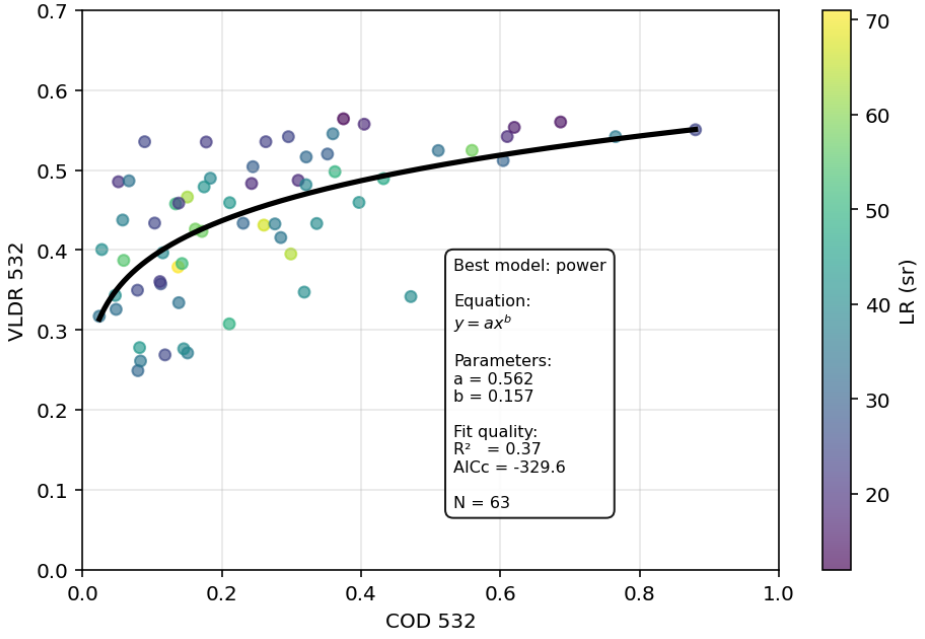

Figure 6. Relationship between cloud optical depth (COD) and volume linear depolarization ratio (VLDR) at 532 nm, with the color bar displaying the lidar ratio retrievals. The solid line indicates the best-fit *power-law* model.

suited for evaluating LACRIT retrievals across different contrail life stages, as it coincided with intense aviation activity and widespread contrail formation over the region. As illustrated in Fig. 7, several persistent contrails formed earlier in the morning were advected into the lidar field of view between 04:00 and 05:30 UTC, enabling the characterization of mature and aged contrails (contrail-induced cirrus). In contrast, the later isolated contrail represents a freshly formed feature, observed within approximately 15 minutes of its formation, providing a complementary view of young contrail properties under the same large-scale atmospheric conditions.

The synoptic meteorological context was characterized using ERA5 reanalysis data. Although not shown here, the wind field exhibited a consistent upper-tropospheric westerly flow throughout the period. Zonal wind speeds increased from approximately 9–11 ms^{-1} at altitudes of 9–10 km to a maximum of about 13–15 ms^{-1} near 11–12 km during the early morning hours (03:30–04:30 UTC). Subsequently, the zonal component weakened, with speeds in the 11–13 km layer decreasing to roughly 10–12 ms^{-1} by 06:30–07:30 UTC. The meridional wind component was predominantly negative, indicating a southward contribution to the flow, with values of approximately -6 to -8 ms^{-1} early in the period, weakening to -1 to -3 ms^{-1} after 06:00 UTC. Together, these values imply a wind vector in the contrail altitude range that initially pointed toward the southeast, before rotating toward a more zonal (west-to-east) direction as the southward component diminished.

Thermodynamically, temperatures ranged from approximately -49 to -55 °C in the lower contrail layer and from -60 to -63 °C in the upper layer, placing both within a regime favorable to persistent ice formation. Calculations of ice relative

https://doi.org/10.5194/egusphere-2026-3056
Preprint. Discussion started: 9 July 2026

humidity further revealed widespread ice-supersaturated regions (ISSR), with values ranging from 125 to 150 % across the analyzed layers. The coexistence of low temperatures, sustained ice supersaturation, and strong upper-tropospheric winds created an environment highly conducive to both the formation and persistence of contrails, as well as their subsequent spreading and aging into contrail-induced cirrus.

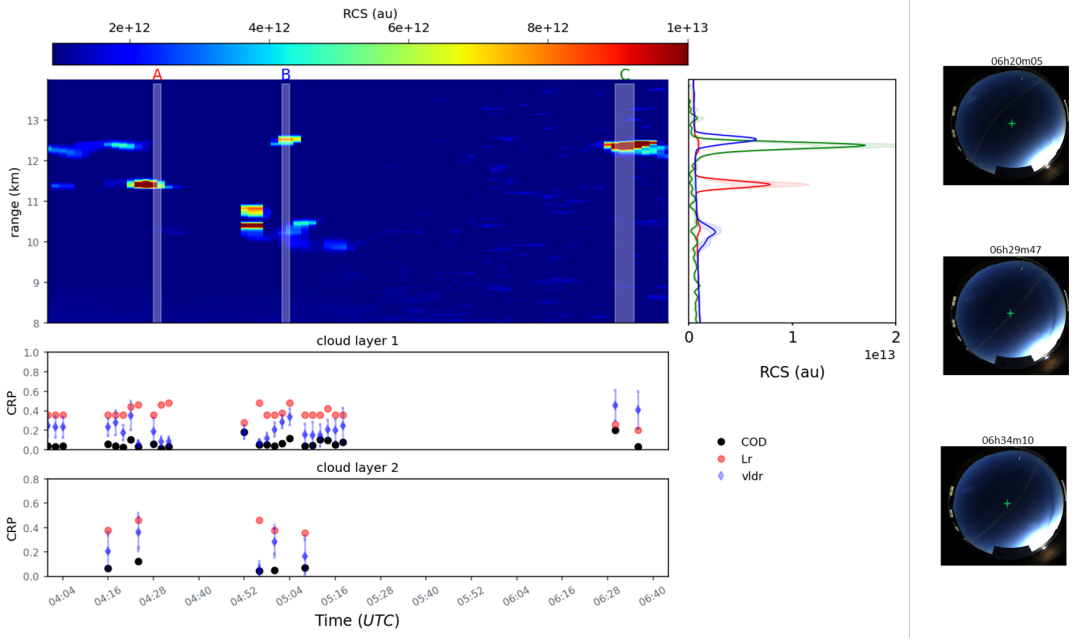

Figure 7. Time–height evolution of the 532-nm range-corrected signal (RCS) during the early-morning period on 6 September 2025, showing multiple advected contrails and an isolated fresh contrail crossing the lidar field of view. Vertical shaded bands (A–C) indicate selected profiles used for detailed analysis; corresponding vertical RCS profiles are shown on the right. Co-located all-sky camera images document the isolated contrail geometry, with the green marker indicating the lidar beam center. The lower panels display the temporal evolution of retrieved COD, LR , and VLDR for the two detected layers, highlighting contrasts between aged advected contrails and a freshly formed, optically thin contrail. The lidar ratio is presented as a fraction of 100 for scaling purposes.

The quantitative statistics summarized in Table 2 highlight the differences in the radiative and microphysical characteristics between advected contrails and isolated fresh contrails. During the early morning period (04:00–05:18 UTC), Layer 1 consistently exhibits low to moderate optical depths for advected subvisible contrails, with a cloud optical depth ranging from 0.04 to 0.08. The lidar ratios during this period varied from 36 to 40 sr. During this period, lidar ratio values reached relatively high levels, comparable to those in natural cirrus and contrail-induced cirrus reported in various studies (Wang et al., 2020; Voudouri et al., 2020; Gouveia et al., 2017; Schroder et al., 2000). Additionally, depolarization ratios (VLDR ≈ 0.19–0.24) are consistent with aged contrail cirrus, where ice crystal growth, aggregation, and habit evolution reduce extinction efficiency relative to backscatter, as highlighted by Iwabuchi et al. 2012. The relatively stable geometrical thicknesses ($H \approx 400$–567 m) suggest vertically coherent layers that have undergone partial dilution while maintaining organized microphysical structures.

https://doi.org/10.5194/egusphere-2026-3056
Preprint. Discussion started: 9 July 2026

Table 2. Summary of radiative and geometrical properties retrieved using the PI method for detected cirrus/contrail layers on 6 September 2025. Reported values correspond to the mean ± standard error of the mean (SEM) within each time block. COD denotes cloud optical depth, VLDR the mean volume linear depolarization ratio, LR the lidar ratio, and H the geometrical thickness of the layer.

Layer	Time interval (UTC)	$\mathrm{COD_{PI}}$	VLDR	$\mathrm{LR_{PI}}$ [sr]	H [m]
L1	04:00–04:04	0.035 ± 0.003	0.24 ± 0.01	36 ± 0	359.8 ± 30.0
L1	04:16–04:30	0.05 ± 0.02	0.20 ± 0.04	40.0 ± 1.9	353.3 ± 23.5
L1	04:50–05:18	0.08 ± 0.01	0.19 ± 0.02	38.0 ± 1.6	567.1 ± 61.5
L1	06:30–06:44	0.12 ± 0.08	0.43 ± 0.02	23.0 ± 3.0	584.6 ± 105.0
L2	04:12–04:20	0.07	0.200	38	344.8
L2	05:00–05:08	0.06 ± 0.01	0.23 ± 0.07	37 ± 2	449.7 ± 89.9

In contrast, the isolated contrail detected later (06:30–06:44 UTC) exhibits markedly different optical and scattering properties despite a comparable mean optical depth ($\mathrm{COD_{PI}} = 0.12 \pm 0.08$). The retrieved lidar ratio decreases to 23.0 ± 3.0 sr, while the depolarization ratio increases to 0.43 ± 0.02, which is consistent with the statistical study of lidar optical properties during the transition from young to mature contrails reported by Iwabuchi et al. (2012). Such a combination of relatively low LR and enhanced depolarization is also consistent with observations of freshly formed contrails dominated by small ice particles, for which extinction efficiency is high relative to backscatter during the early growth stage (Sassen and Cho, 1992; Schumann and Heymsfield, 2017; Atlas and Wang, 2010; Schroder et al., 2000). In this regime, modest changes in particle habit or orientation can significantly affect the depolarization signal, while the backscatter-to-extinction ratio remains relatively low prior to substantial particle growth or aggregation.

The geometrical thickness of the isolated contrail ($H \approx 584.6$ m) is comparable to that of the earlier advected layers, suggesting that the observed differences in LR and depolarization are primarily linked to microphysical evolution rather than to geometrical effects alone. Similar contrasts between fresh and aged contrails have been reported in lidar-based case studies and climatological analyses, highlighting the rapid evolution of ice-crystal properties during the first tens of minutes following contrail formation (Febvre et al., 2009; Schumann and Heymsfield, 2017; Chauvigné et al., 2018).

For layer 2, the retrieved CRP are broadly consistent with those obtained for layer 1 during the same observation period. Our results agree with observational studies reporting cirrus lidar ratios in the upper troposphere and near the tropopause, where typical values range between 20 and 40 sr and tend to decrease with increasing altitude (and decreasing temperature) (Chen et al., 2002). The limited number of lidar-ratio retrievals in layer 2 highlights the increased sensitivity of the measurements in very thin cloud structures, where the contribution of the molecular background relative to the weak particulate signal, together with low signal-to-noise ratios (SNR), can significantly affect the stability of the retrieval.

https://doi.org/10.5194/egusphere-2026-3056
Preprint. Discussion started: 9 July 2026

5 Conclusions

This study introduces a comprehensive ground-based framework designed for the detection and characterization of the radiative properties of natural cirrus clouds and contrail-induced clouds. The framework integrates co-located elastic lidar with depolarization capabilities, a microwave radiometer, and observations from an all-sky camera, all situated in Toulouse, France. A significant contribution of this research is the retrieval framework, which encompasses effective layer detection, transmittance-based optical depth estimation, and a modified version of the integration approach proposed by Cadet et al. 2005. This modification enables the determination of the lidar ratio through an iterative method specifically tailored for use within the optically thin to subvisible cirrus regime.

The layer detection strategy has proven effective in isolating thin cloud layers while minimizing noise-driven detections in near-molecular conditions. For the example cases presented, this approach allowed for stable identification of cloud boundaries and reliable estimation of transmittance, even for cloud optical depths below 0.05. The close agreement observed between transmittance-based and particle integration optical depths, with relative discrepancies ranging from 1% to 4%, demonstrated the internal consistency of the retrieval process. This also supported the validity of the corrected particle integration formulation with consistent altitude indexing.

The application of this method to both cirrus and contrail cases underscores the strong sensitivity of the lidar ratio to the cloud microphysical state and thermodynamics, which vary depending on the detection altitude. Notable differences in cirrus were observed, particularly in optically thin layers. For similar optical depths, significant variations in the lidar ratio were obatained between layers formed at different altitudes, as well as between aged and freshly formed contrails. The analysis of the isolated contrail case further illustrates the effectiveness of combined lidar and camera observations in distinguishing the evolutionary stages of contrails under comparable large-scale meteorological conditions. Specifically, the isolated contrail, measured by lidar approximately 15 minutes after formation, exhibited a lower lidar ratio and a depolarization of around 23 sr and 43%, respectively, in contrast to the advected, aged contrail cirrus. This aligns with expectations for small, weakly aggregated ice particles before they experience significant microphysical aging. These findings emphasize the importance of temporally and range resolved observations for disentangling the effects of contrail age and accurately interpreting the retrieved radiative properties.

This study demonstrates that robust lidar-based retrievals, when integrated with complementary passive observations, offer valuable insights into the radiative properties of cirrus and contrail-induced clouds. The LACRIT framework provides a flexible and physically consistent tool for constructing long-term datasets of thin-cloud radiative properties. Such datasets are essential for evaluating contrail–cirrus parameterizations and for minimizing uncertainties in assessments of aviation-induced climate forcing. Future work will concentrate on expanding the statistical analysis to encompass the complete record of measurements collected over the past years. This will involve integrating the retrievals with flight trajectory data and directly connecting the observations to contrail and cirrus modeling frameworks. The objectives include: i) studying the relationships between ice supersaturated regions and the radiative and microphysical properties of contrails, ii) exploring the spectral dependence of the retrieved products, and iii) assessing the sensitivity of the method using a large dataset.

https://doi.org/10.5194/egusphere-2026-3056
Preprint. Discussion started: 9 July 2026

Code and data availability. The datasets and processing scripts used in this study are available from the corresponding author upon reasonable request.

Author contributions. AEBV developed the LACRIT algorithm, processed the lidar and ancillary datasets, performed the analysis, and wrote the original manuscript draft. RC, CS, and CP contributed to the methodology, interpretation of the results, and scientific discussion, and reviewed and edited the manuscript. All authors discussed the results and contributed to the final version of the manuscript.

Competing interests. The authors declare that they have no conflict of interest.

Disclaimer. Views and opinions expressed are, however, those of the authors only and do not necessarily reflect those of the European Union or the European Research Executive Agency. Neither the European Union nor the European Research Executive Agency can be held responsible for them.

Acknowledgements. The authors acknowledge the support of the DGAC and the Horizon Europe programme under the Marie Skłodowska-Curie Staff Exchange Actions with the project AERIS (grant agreement No. 101236396). This research has received funding from the SESAR 3 Joint Undertaking under grant agreement No. 101114613 (CICONIA) under the European Union's Horizon Europe research and innovation programme. The authors acknowledge their use of AI-based editing tools, including Grammarly and ChatGPT, to enhance the manuscript's clarity, readability, and grammar.

https://doi.org/10.5194/egusphere-2026-3056
Preprint. Discussion started: 9 July 2026

References

Ansmann, A., Riebesell, M., and Weitkamp, C.: Measurement of atmospheric aerosol extinction profiles with a Raman lidar, Applied Optics, 31, 7113–7131, https://doi.org/10.1364/AO.31.007113, 1992.

Antuña-Sánchez, J. C., Román, R., Bosch, J. L., Toledano, C., Mateos, D., González, R., Cachorro, V., and de Frutos, : ORION software tool for the geometrical calibration of all-sky cameras, PLOS ONE, 17, 1–17, https://doi.org/10.1371/journal.pone.0265959, 2022.

Atlas, D. and Wang, Z.: Contrails of Small and Very Large Optical Depth, Journal of the Atmospheric Sciences, 67, 3065 – 3073, https://doi.org/10.1175/2010JAS3403.1, 2010.

Bock, L. and Burkhardt, U.: Contrail cirrus radiative forcing for future air traffic, Atmospheric Chemistry and Physics, 19, 8163–8174, https://doi.org/10.5194/acp-19-8163-2019, 2019.

Cadet, B., Giraud, V., Haeffelin, M., Keckhut, P., Rechou, A., and Baldy, S.: Improved retrievals of the optical properties of cirrus clouds by a combination of lidar methods, Appl. Opt., 44, 1726–1734, https://doi.org/10.1364/AO.44.001726, 2005.

Chauvigné, A., Jourdan, O., Schwarzenboeck, A., Gourbeyre, C., Gayet, J. F., Voigt, C., Schlager, H., Kaufmann, S., Borrmann, S., Molleker, S., Minikin, A., Jurkat, T., and Schumann, U.: Statistical analysis of contrail to cirrus evolution during the Contrail and Cirrus Experiment (CONCERT), Atmospheric Chemistry and Physics, 18, 9803–9822, https://doi.org/10.5194/acp-18-9803-2018, 2018.

Chen, W.-N., Chiang, C.-W., and Nee, J.-B.: Lidar ratio and depolarization ratio for cirrus clouds, Appl. Opt., 41, 6470–6476, https://doi.org/10.1364/AO.41.006470, 2002.

Chepfer, H., Goloub, P., Riedi, J., et al.: Ice crystal shapes in cirrus clouds derived from POLDER/ADEOS-1, Journal of Geophysical Research, 109, https://doi.org/10.1029/2004JD004706, 2004.

Comstock, J. M. and Sassen, K.: Retrieval of Cirrus Cloud Radiative and Backscattering Properties Using Combined Lidar and Infrared Radiometer (LIRAD) Measurements, Journal of Atmospheric and Oceanic Technology, 18, 1658 – 1673, https://doi.org/10.1175/1520-0426(2001)018<1658:ROCCRA>2.0.CO;2, 2001.

Dionisi, D., Keckhut, P., Liberti, G. L., Cardillo, F., and Congeduti, F.: Midlatitude cirrus classification at Rome Tor Vergata through a multichannel Raman–Mie–Rayleigh lidar, Atmospheric Chemistry and Physics, 13, 11 853–11 868, https://doi.org/10.5194/acp-13-11853-2013, 2013.

Febvre, G., Gayet, J.-F., Minikin, A., Schlager, H., Shcherbakov, V., Jourdan, O., Busen, R., Fiebig, M., Kärcher, B., and Schumann, U.: On optical and microphysical characteristics of contrails and cirrus, Journal of Geophysical Research: Atmospheres, 114, https://doi.org/https://doi.org/10.1029/2008JD010184, 2009.

Freudenthaler, V., Jäger, H., and Homburg, F.: Optical parameters of contrails from lidar measurements, Journal of Atmospheric and Oceanic Technology, 13, 435–447, https://doi.org/10.1175/1520-0426(1996)013<0435:OPOCFL>2.0.CO;2, 1996.

Gil-Díaz, C., Sicard, M., Comerón, A., dos Santos Oliveira, D. C. F., Muñoz Porcar, C., Rodríguez-Gómez, A., Lewis, J. R., Welton, E. J., and Lolli, S.: Geometrical and optical properties of cirrus clouds in Barcelona, Spain: analysis with the two-way transmittance method of 4 years of lidar measurements, Atmospheric Measurement Techniques, 17, 1197–1216, https://doi.org/10.5194/amt-17-1197-2024, 2024.

Gouveia, D. A., Barja, B., Barbosa, H. M. J., Seifert, P., Baars, H., Pauliquevis, T., and Artaxo, P.: Optical and geometrical properties of cirrus clouds in Amazonia derived from 1 year of ground-based lidar measurements, Atmospheric Chemistry and Physics, 17, 3619–3636, https://doi.org/10.5194/acp-17-3619-2017, 2017.

https://doi.org/10.5194/egusphere-2026-3056
Preprint. Discussion started: 9 July 2026

Hlavka, D. L., Yorks, J. E., Young, S. A., Vaughan, M. A., Kuehn, R. E., McGill, M. J., and Rodier, S. D.: Airborne validation of cirrus cloud properties derived from CALIPSO lidar measurements: Optical properties, Journal of Geophysical Research: Atmospheres, 117, https://doi.org/https://doi.org/10.1029/2011JD017053, 2012.

Immler, F. and Schrems, O.: Lidar measurements of cirrus clouds in the northern midlatitudes, Atmospheric Chemistry and Physics, 7, 3565–3578, https://doi.org/10.5194/acp-7-3565-2007, 2007.

Iwabuchi, H., Yang, P., Liou, K. N., and Minnis, P.: Physical and optical properties of persistent contrails: Climatology and interpretation, Journal of Geophysical Research: Atmospheres, 117, https://doi.org/https://doi.org/10.1029/2011JD017020, 2012.

Kärcher, B., Burkhardt, U., and Unterstrasser, S.: Importance of representing optical depth variability for estimates of contrail radiative forcing, Proceedings of the National Academy of Sciences, 106, 19 107–19 112, https://doi.org/10.1073/pnas.0902106106, 2009.

Klett, J. D.: Stable analytical inversion solution for processing lidar returns, Appl. Opt., 20, 211–220, https://doi.org/10.1364/AO.20.000211, 1981.

Klett, J. D.: Lidar inversion with variable backscatter/extinction ratios, Appl. Opt., 24, 1638–1643, https://doi.org/10.1364/AO.24.001638, 1985.

Kustova, N., Konoshonkin, A., Shishko, V., Timofeev, D., Tkachev, I., Wang, Z., and Borovoi, A.: Depolarization Ratio for Randomly Oriented Ice Crystals of Cirrus Clouds, Atmosphere, 13, https://doi.org/10.3390/atmos13101551, 2022.

Lee, D., Fahey, D., Skowron, A., Allen, M., Burkhardt, U., Chen, Q., Doherty, S., Freeman, S., Forster, P., Fuglestvedt, J., Gettelman, A., De León, R., Lim, L., Lund, M., Millar, R., Owen, B., Penner, J., Pitari, G., Prather, M., Sausen, R., and Wilcox, L.: The contribution of global aviation to anthropogenic climate forcing for 2000 to 2018, Atmospheric Environment, 244, 117 834, https://doi.org/https://doi.org/10.1016/j.atmosenv.2020.117834, 2021.

Li, Q. and Groß, S.: Lidar observations of cirrus cloud properties with CALIPSO from midlatitudes towards high-latitudes, Atmospheric Chemistry and Physics, 25, 16 657–16 677, https://doi.org/10.5194/acp-25-16657-2025, 2025.

Martucci, G., Milroy, C., and O'Dowd, C. D.: Detection of Cloud-Base Height Using Jenoptik CHM15K and Vaisala CL31 Ceilometers, Journal of Atmospheric and Oceanic Technology, 27, 305–318, https://doi.org/10.1175/2009JTECHA1326.1, 2010.

Mitchell, D. L., Garnier, A., and Woods, S.: Advances in CALIPSO (IIR) cirrus cloud property retrievals – Part 1: Methods and testing, Atmospheric Chemistry and Physics, 25, 14 071–14 098, https://doi.org/10.5194/acp-25-14071-2025, 2025.

Ng, J. Y.-H., McCloskey, K., Cui, J., Meijer, V. R., Brand, E., Sarna, A., Goyal, N., Van Arsdale, C., and Geraedts, S.: Contrail Detection on GOES-16 ABI With the OpenContrails Dataset, IEEE Transactions on Geoscience and Remote Sensing, 62, 1–14, https://doi.org/10.1109/TGRS.2023.3345226, 2024.

Noel, V., Chepfer, H., Ledanois, G., Delaval, A., and Flamant, P. H.: Classification of particle effective shape ratios in cirrus clouds based on the lidar depolarization ratio, Appl. Opt., 41, 4245–4257, https://doi.org/10.1364/AO.41.004245, 2002.

Platt, C. M. R., Young, S. A., Carswell, A. I., and Pal, S. R.: The optical properties of cirrus clouds, Journal of Geophysical Research, 99, 22 901–22 911, https://doi.org/10.1029/94JD01705, 1994.

Popovici, I. E., Goloub, P., Podvin, T., Blarel, L., Loisil, R., Unga, F., Mortier, A., Deroo, C., Victori, S., Ducos, F., Torres, B., Delegove, C., Choël, M., Pujol-Söhne, N., and Pietras, C.: Description and applications of a mobile system performing on-road aerosol remote sensing and in situ measurements, Atmospheric Measurement Techniques, 11, 4671–4691, https://doi.org/10.5194/amt-11-4671-2018, 2018.

Sanchez Barrero, M. F., Popovici, I. E., Goloub, P., Victori, S., Hu, Q., Torres, B., Podvin, T., Blarel, L., Dubois, G., Ducos, F., Bourrianne, E., Lapionak, A., Proniewski, L., Holben, B., Giles, D. M., and LaRosa, A.: Enhancing mobile aerosol monitoring with CE376

https://doi.org/10.5194/egusphere-2026-3056
Preprint. Discussion started: 9 July 2026

dual-wavelength depolarization lidar, Atmospheric Measurement Techniques, 17, 3121–3146, https://doi.org/10.5194/amt-17-3121-2024, 2024.

Sassen, K. and Cho, B. S.: Subvisual-Thin Cirrus Lidar Dataset for Satellite Verification and Climatological Research, Journal of Applied Meteorology and Climatology, 31, 1275 – 1285, https://doi.org/10.1175/1520-0450(1992)031<1275:STCLDF>2.0.CO;2, 1992.

Schroder, F., K?rcher, B., Duroure, C., Str?m, J., Petzold, A., Gayet, J.-F., Strauss, B., Wendling, P., and Borrmann, S.: On the Transition of Contrails into Cirrus Clouds, Journal of the Atmospheric Sciences, 57, 464 – 480, https://doi.org/10.1175/1520-0469(2000)057<0464:OTTOCI>2.0.CO;2, 2000.

Schumann, U.: A contrail cirrus prediction model, Geoscientific Model Development, 5, 543–580, https://doi.org/10.5194/gmd-5-543-2012, 2012.

Schumann, U. and Heymsfield, A. J.: On the Life Cycle of Individual Contrails and Contrail Cirrus, Meteorological Monographs, 58, 3.1 – 3.24, https://doi.org/10.1175/AMSMONOGRAPHS-D-16-0005.1, 2017.

Urbanek, B., Groß, S., Wirth, M., Rolf, C., Krämer, M., and Voigt, C.: High Depolarization Ratios of Naturally Occurring Cirrus Clouds Near Air Traffic Regions Over Europe, Geophysical Research Letters, 45, 13,166–13,172, https://doi.org/https://doi.org/10.1029/2018GL079345, 2018.

Voudouri, K. A., Giannakaki, E., Komppula, M., and Balis, D.: Variability in cirrus cloud properties using a Polly^{XT} Raman lidar over high and tropical latitudes, Atmospheric Chemistry and Physics, 20, 4427–4444, https://doi.org/10.5194/acp-20-4427-2020, 2020.

Wang, W., Yi, F., Liu, F., Zhang, Y., Yu, C., and Yin, Z.: Characteristics and Seasonal Variations of Cirrus Clouds from Polarization Lidar Observations at a 30°N Plain Site, Remote Sensing, 12, https://doi.org/10.3390/rs12233998, 2020.

Yorks, J. E., Hlavka, D. L., Hart, W. D., and McGill, M. J.: Statistics of Cloud Optical Properties from Airborne Lidar Measurements, Journal of Atmospheric and Oceanic Technology, 28, 869 – 883, https://doi.org/10.1175/2011JTECHA1507.1, 2011.

Zhou, C., Yang, P., Dessler, A. E., Hu, Y., and Baum, B. A.: Study of Horizontally Oriented Ice Crystals with CALIPSO Observations and Comparison with Monte Carlo Radiative Transfer Simulations, Journal of Applied Meteorology and Climatology, 51, 1426 – 1439, https://doi.org/10.1175/JAMC-D-11-0265.1, 2012.